ALMA Survey of Orion Planck Galactic Cold Clumps (ALMASOP): A Forming Quadruple System with Continuum "Ribbons" and Intricate Outflows

Luo, Qiu-yi, Liu, Tie, Lee, Aaron T., Offner, Stella S. R., di Francesco, James, Johnstone, Doug, Juvela, Mika, Goldsmith, Paul F., Qin, Sheng-Li, Mai, Xiaofeng, Liu, Xun-chuan, Sanhueza, Patricio, Xu, Feng-Wei, Tatematsu, Ken'ichi, Dutta, Somnath, Chen, Huei-Ru Vivien, Li, Shanghuo, Yang, Aiyuan, Liu, Sheng-Yuan, Lee, Chin-Fei, Hirano, Naomi, Lee, Chang Won, Sahu, Dipen, Shang, Hsien, Hsu, Shih-Ying, Bronfman, Leonardo, Kwon, Woojin, Rawlings, M. G., Eden, David, Lu, Xing, Gu, Qi-lao, Ren, Zhiyuan, Ward-Thompson, Derek and Shen, Zhi-Qiang

Luo, Qiu-yi, Liu, Tie, Lee, Aaron T., Offner, Stella S. R., di Francesco, James, Johnstone, Doug, Juvela, Mika, Goldsmith, Paul F., Qin, Sheng-Li et al (2023) ALMA Survey of Orion Planck Galactic Cold Clumps (ALMASOP): A Forming Quadruple System with Continuum "Ribbons" and Intricate Outflows. Astrophysical Journal Letters, 952 (1). ISSN 2041-8205

The Astrophysical Journal Letters, 952:L2 (10pp), 2023 July 20 https://doi.org/10.3847/2041-8213/acdddf

ALMA Survey of Orion Planck Galactic Cold Clumps (ALMASOP): A Forming Quadruple System with Continuum "Ribbons" and Intricate Outflows

Qiu-yi Luo[1,2], Tie Liu[1], Aaron T. Lee[3], Stella S. R. Offner[4], James di Francesco[5,6], Doug Johnstone[5,6], Mika Juvela[7], Paul F. Goldsmith[8], Sheng-Li Qin[9], Xiaofeng Mai[1,2], Xun-chuan Liu[1], Patricio Sanhueza[10,11], Feng-Wei Xu[12,13], Ken'ichi Tatematsu[14,15], Somnath Dutta[16], Huei-Ru Vivien Chen[17], Shanghuo Li[18], Aiyuan Yang[19], Sheng-Yuan Liu[16], Chin-Fei Lee[16], Naomi Hirano[16], Chang Won Lee[20,21], Dipen Sahu[16,22], Hsien Shang[16], Shih-Ying Hsu[16], Leonardo Bronfman[23], Woojin Kwon[24,25], M. G. Rawlings[26], David Eden[27], Xing Lu[1], Qi-lao Gu[1], Zhiyuan Ren[28], D. Ward-Thompson[29], and Zhi-Qiang Shen[1]

[1] Shanghai Astronomical Observatory, Chinese Academy of Sciences, 80 Nandan Road, Shanghai 200030, People's Republic of China; lqy@shao.ac.cn, liutie@shao.ac.cn
[2] School of Astronomy and Space Sciences, University of Chinese Academy of Sciences, No. 19A Yuquan Road, Beijing 100049, People's Republic of China
[3] Department of Physics and Astronomy, Saint Mary's College of California, 1928 Saint Mary's Road, Moraga, CA 94575, USA
[4] Department of Astronomy, University of Texas Austin, Austin, TX 78712, USA
[5] NRC Herzberg Astronomy and Astrophysics, 5071 West Saanich Road, Victoria, BC, V9E 2E7, Canada
[6] Department of Physics and Astronomy, University of Victoria, 3800 Finnerty Road, Elliot Building, Victoria, BC, V8P 5C2, Canada
[7] Department of Physics, P.O. Box 64, FI-00014, University of Helsinki, Finland
[8] Jet Propulsion Laboratory, California Institute of Technology, Pasadena, CA 91109, USA
[9] Department of Astronomy, Yunnan University, Kunming 650091, People's Republic of China
[10] National Astronomical Observatory of Japan, National Institutes of Natural Sciences, 2-21-1 Osawa, Mitaka, Tokyo 181-8588, Japan
[11] Department of Astronomical Science, SOKENDAI (The Graduate University for Advanced Studies), 2-21-1 Osawa, Mitaka, Tokyo 181-8588, Japan
[12] Department of Astronomy, School of Physics, Peking University, Beijing 100871, People's Republic of China
[13] Kavli Institute for Astronomy and Astrophysics, Peking University, Haidian District, Beijing 100871, People's Republic of China
[14] Nobeyama Radio Observatory, National Astronomical Observatory of Japan, National Institutes of Natural Sciences, Nobeyama, Minamimaki, Minamisaku, Nagano 384-1305, Japan
[15] Astronomical Science Program, Graduate Institute for Advanced Studies, SOKENDAI,2-21-1 Osawa, Mitaka, Tokyo 181-8588, Japan
[16] Academia Sinica Institute of Astronomy and Astrophysics, 11F of AS/NTU Astronomy-Mathematics Building, No.1, Sec. 4, Roosevelt Rd, Taipei 10617, Taiwan
[17] Institute of Astronomy and Department of Physics, National Tsing Hua University, Hsinchu, Taiwan
[18] Max Planck Institute for Astronomy, Königstuhl 17, D-69117 Heidelberg, Germany
[19] National Astronomical Observatories, Chinese Academy of Sciences, A20 Datun Road, Chaoyang District, Beijing 100101, People's Republic of China
[20] Korea Astronomy and Space Science Institute, 776 Daedeokdae-ro, Yuseong-gu, Daejeon 34055, Republic of Korea
[21] University of Science and Technology, Korea (UST), 217 Gajeong-ro, Yuseong-gu, Daejeon 34113, Republic of Korea
[22] Physical Research laboratory, Navrangpura, Ahmedabad, Gujarat 380009, India
[23] Departamento de Astronomía, Universidad de Chile, Las Condes, 7591245 Santiago, Chile
[24] Department of Earth Science Education, Seoul National University, 1 Gwanak-ro, Gwanak-gu, Seoul 08826, Republic of Korea
[25] SNU Astronomy Research Center, Seoul National University, 1 Gwanak-ro, Gwanak-gu, Seoul 08826, Republic of Korea
[26] Gemini Observatory/NSF's NOIRLab, 670 N. A'ohoku Place, Hilo, HI 96720, USA
[27] Armagh Observatory and Planetarium, College Hill, Armagh, BT61 9DB, UK
[28] National Astronomical Observatories, Chinese Academy of Sciences, Datun Rd. A20, Beijing, People's Republic of China
[29] Jeremiah Horrocks Institute, UCLAN, Preston, PR1 2HE, UK
[30] Institute of Astronomy and Astrophysics, Academia Sinica, Taipei 10617, Taiwan
Received 2023 April 5; revised 2023 June 12; accepted 2023 June 13; published 2023 July 18

Abstract

One of the most poorly understood aspects of low-mass star formation is how multiple-star systems are formed. Here we present the results of Atacama Large Millimeter/submillimeter Array (ALMA) Band 6 observations toward a forming quadruple protostellar system, G206.93-16.61E2, in the Orion B molecular cloud. ALMA 1.3 mm continuum emission reveals four compact objects, of which two are Class I young stellar objects and the other two are likely in prestellar phase. The 1.3 mm continuum emission also shows three asymmetric ribbon-like structures that are connected to the four objects, with lengths ranging from ∼500 to ∼2200 au. By comparing our data with magnetohydrodynamic simulations, we suggest that these ribbons trace accretion flows and also function as gas bridges connecting the member protostars. Additionally, ALMA CO $J = 2-1$ line emission reveals a complicated molecular outflow associated with G206.93-16.61E2, with arc-like structures suggestive of an outflow cavity viewed pole-on.

Unified Astronomy Thesaurus concepts: Star formation (1569); Star forming regions (1565); Multiple stars (1081); Interstellar medium (847); Protostars (1302)

1. Introduction

Approximately half of the stars in the Galaxy reside in systems with two or more stars, with the multiplicity fraction for low-mass M stars being about one-third (Duchêne & Kraus 2013; Offner et al. 2022). Near-infrared and submillimeter continuum observations toward star-forming regions in nearby molecular clouds have revealed that ∼28% to ∼64% of low-mass protostars are found in multiple systems, with typical separations of 100–8900 au between members (Offner et al. 2022). Most of these young stellar systems, however, are binary systems, while higher-order systems are rare (Chen et al. 2013; Kounkel et al. 2016; Tobin et al. 2016, 2022; Luo et al. 2022). Moreover, it is hard to determine whether higher-order systems are gravitationally bound based on continuum observations alone. Pineda et al. (2015) found a forming quadruple star system in the Barnard 5 dense core using NH_3 observations taken by the Very Large Array. The authors argued that Barnard 5 hosts a gravitationally bound system containing one protostar and three prestellar condensations with separations of a few thousand astronomical units. A dynamic analysis suggested that two wide-separated members in the systems will likely become unbound after formation.

Forming multiple systems are often observed to contain extended dynamic structures, such as gas streamers, and gas bridges connecting the members. The gas distribution and associated protostellar outflows in such systems are usually very complicated and thus difficult to interpret. For example, the condensations in the Barnard 5 region are embedded in dense gas streamers (Pineda et al. 2015). Similar gas streamers have been witnessed in recent submillimeter observations toward other star-forming regions. In general, these gas streamers are asymmetric, with lengths of several to thousands of astronomical units (Takakuwa et al. 2017; Keppler et al. 2020; Rosotti et al. 2020). Pineda et al. (2020) found a 10,500 au gas streamer in the Per-emb-2 dense core, which appears to be delivering material from the outer dense core to the inner disk. Computationally, a number of magnetohydrodynamic (MHD) simulations have reproduced asymmetric streamers, e.g., gas bridges, which can be attributed to dynamical interaction between protostar members. For example, simulated flybys (Kratter et al. 2010; Clark et al. 2011; Kuffmeier et al. 2019; Dong et al. 2022) produce bridges, though these bridge structures are caused by interactions between the forming stars, not the flyby per se. Finally, observations of multiple protostellar systems have shown noncollimated, asymmetric, and complex outflow structures (Kwon et al. 2015; Oya et al. 2021). Hence, analyzing and understanding the dynamic mechanism of outflows and gas streamers is essential to unveiling the mystery of higher-order star system formation.

G206.93-16.61E2 is a protostellar core (Yi et al. 2018) close to the reflection nebula NGC 2023 in the Orion B molecular cloud (at a distance of 407 ± 4 pc; Kounkel et al. 2018). The core is associated with the infrared source 2MASS J05413704-0217178, also known as HOPS-298 (Megeath et al. 2012; Furlan et al. 2016). Recent Atacama Large Millimeter/submillimeter Array (ALMA) Band 7 observations have resolved HOPS-298 into two Class I protostars (A, B) at a resolution of 0.″1 (Tobin et al. 2020). Besides these two protostars, the 1.3 mm continuum emission obtained by the ALMA Survey of Orion Planck Galactic Cold Clumps (ALMASOP) project further revealed two additional gas condensations within this core (Dutta et al. 2020; Luo et al. 2022).

In this paper, we present spatially resolved observations of 1.3 mm continuum, CO $J = 2-1$, $C^{18}O$ ($J = 2-1$), SiO ($J = 5-4$), and H_2CO ($J = 3-2$) line emission toward G206.93-16.61E2. Our observations capture the presence of apparent streamer-like structures in the dust continuum emission. In addition, we detect an outflow with a highly intricate dynamic behavior that has not been previously reported. The paper is organized as follows: in Section 2, we describe the observations and data reduction. In Section 3, we present the observational results. We then discuss the origin of the quadruple system in Section 4. Finally, we summarize the conclusions in Section 5.

2. Observations

G206.93-16.61E2 was observed with ALMA at Band 6 from 2018 October to 2019 January as part of the ALMASOP project (project ID: 2018.1.00302.S; PI: Tie Liu). The observations were conducted with the 12 m array in its C43-5 (TM1) and C43-2 (TM2) configurations, and with the Atacama Compact Array (ACA). The receivers were set up to cover four individual spectral windows (centered at 216.6, 218.9, 231.0, and 233.0 GHz), each with a bandwidth of 1.875 GHz and a velocity resolution of 1.4 km s^{-1}. Molecular lines, including CO ($J = 2-1$), $C^{18}O$ ($J = 2-1$), H_2CO $J = 3-2$, N_2D^+ ($J = 3-2$), DCO^+ ($J = 3-2$), DCN ($J = 3-2$), and SiO ($J = 5-4$), were simultaneously observed. These line emission channels were removed from the ensemble of data used to make a continuum image. In this paper, we present the results of the 1.3 mm continuum, CO ($J = 2-1$), $C^{18}O$ ($J = 2-1$), SiO ($J = 5-4$), and H_2CO ($J = 3-2$) line emission data.

We performed the calibration and data imaging using the Common Astronomy Software Application (CASA) Version 5.4 (McMullin et al. 2007). The calibrated data were imaged with the TCLEAN task by combining data from all three configurations (TM1, TM2, and ACA), with a robust Briggs parameter of 0.5. More details of the data reduction are described by Dutta et al. (2020) and Sahu et al. (2021, 2023). The largest angular recoverable scale is ∼25″ and the field of view (FOV) of the final images is about 40″. The synthesized beam is 0.″38 × 0.″33 (152 au × 132 au) and the sensitivity is ∼0.15 mJy $beam^{-1}$ in the 1.3 mm dust continuum emission. The final synthesized beam of ^{12}CO $J = 2-1$ is 0.″36 × 0.″31 (144 au × 124 au), based on the same setting, and the observations have an rms noise of 3 mJy $beam^{-1}$ per channel.

3. Results

3.1. A Forming Quadruple Stellar System

Figure 1 shows the infrared and the dust continuum emission maps for the G206.93-16.62E2 dense core obtained with various instruments. In Figure 1(b), ALMA 1.3 mm observations spatially resolve four compact sources, which were previously reported by Dutta et al. (2020). The two point sources G206.93-16.61E2_A and G206.93-16.61E2_B (hereafter, E2_A and E2_B, respectively) correspond to the two Class I protostars, HOPS-298-A and HOP-298-B (projected separation ∼950 au), as also classified by Tobin et al. (2020). The other two fainter and diffuse condensations, G206.93-16.61E2_C (E2_C) and G206.93-16.61E2_D (E2_D), were not detected by Tobin et al. (2020). Three of the sources—E2_A, E2_C, and E2_D—are in close proximity to each other, with a mean projected separation of about 450 au. The projected separations between protostar E2_B and the three other sources (E2_A, E2_C, and E2_D) are 950 au, 1250 au, and 900 au, respectively.

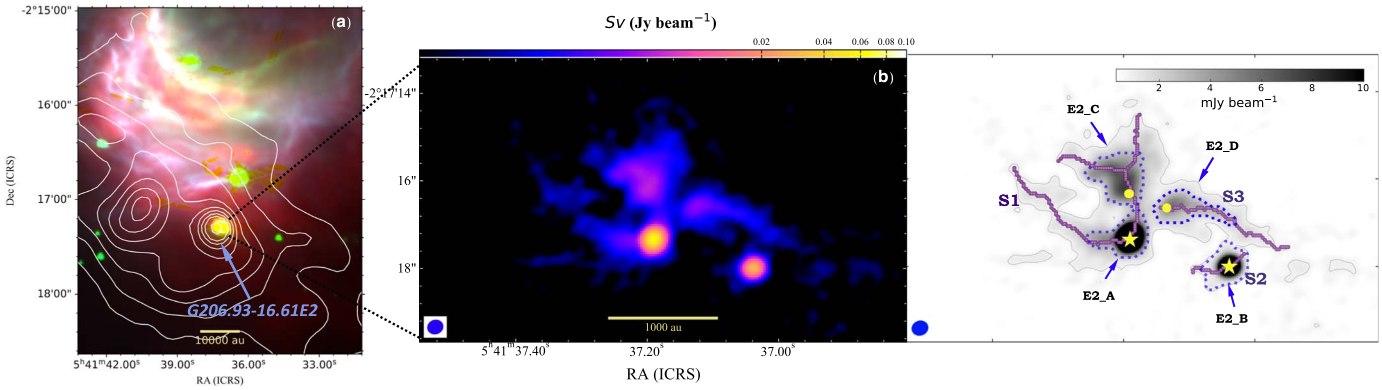

Figure 1. Dense core G206.93-16.61E2. (a) JCMT SCUBA-2 850 μm in contours overlaid on RGB image of Herschel 100 μm (red) and Spitzer 4.5 (green) and 8 μm (blue) data. The contours are given in white from $4\sigma_{0.85\ \mathrm{mm}}$ to $28\sigma_{0.85\ \mathrm{mm}}$, with a step of $4\sigma_{0.85\ \mathrm{mm}}$ ($1\sigma_{0.85\ \mathrm{mm}} = 25$ mJy beam^{-1}). (b) Left: ALMA 1.3 mm dust continuum image. Right: the same image with one contour at the $5\sigma_{1.3\ \mathrm{mm}}$ level in gray ($1\sigma_{1.3\ \mathrm{mm}} = 0.15$ mJy beam^{-1}). The blue dotted lines indicate the leaf structures, identified by Astrodendro, surrounding the sources E2_A, E2_B, E2_C, and E2_D. The yellow symbols indicate the locations of the peak intensity in each structure. The yellow stars represent the two YSOs (E2_A and E2_B, also known as HOPS-298-A and B) and the yellow circles represent the two gas condensations (E2_C and E2_D). The continuum "ribbon" structures are indicated by purple lines.

Table 1
Properties of Members of G206.93-16.61E2

Source ID (1)	R.A. (J2000) (hh:mm:ss) (2)	Decl. (J2000) (dd:mm:ss) (3)	Flux Density (mJy) (4)	Radius (au) (5)	M_{gas} ($M_{\odot}$) (6)	M_{vir} ($M_{\odot}$) (7)	α (8)
G206.93-16.61E2_A	05:41:37.19	−02:17:17.34	97	147	0.26	0.31	1.19
G206.93-16.61E2_B	05:41:37.04	−02:17:17.99	39	148	0.10	0.31	3.10
G206.93-16.61E2_C	05:41:37.20	−02:17:15.97	40	142	0.39	0.18	0.46
G206.93-16.61E2_D	05:41:37.15	−02:17:16.52	19	141	0.19	0.19	1.00

Note. Columns (1)–(3): names and coordinates of objects in G206.93-16.61E2, taken from Dutta et al. (2020). Columns (4)–(5): flux density and deconvolved radius of each object extracted from Astrodendro. Columns (6)–(8): gas masses, virial masses, and virial parameters are derived assuming a dust temperature of 25 K for protostellar objects and 10 K for starless objects (as discussed in Appendix A, if the dust temperature of the starless objects is 25 K, then M_{gas} decreases, M_{vir} increases, and α increases). Gravitational collapse is expected when $\alpha < 2$.

We utilize the Astrodendro Python package[31] to identify the boundaries of each source. We adopt the min_value = $3\sigma_{1.3\ \mathrm{mm}}$ ($1\sigma_{1.3\ \mathrm{mm}}$= 0.15 mJy beam^{-1}), min_delta = $1\sigma_{1.3\ \mathrm{mm}}$, and min_npix = 18. The four members are defined by the smallest substructures, "leaf" structures, in the 1.3 mm dust continuum emission above the 5σ threshold found by Astrodendro. The resulting boundaries of these four sources are shown by the blue dotted shapes in the right panel of Figure 1(b). The four members are almost contiguous and embedded within a common gas envelope. Table 1 lists the coordinates, flux densities, and deconvolved radii of these sources, as extracted from Astrodendro.

To determine whether the four individual sources are gravitationally bound, we use the "leaf" boundaries derived above for each to derive the 1.3 mm continuum–based gas mass M_{gas}, virial mass M_{vir}, and virial parameter α (see Appendix A), which are also listed in Table 1. The gas masses (M_{gas}) of the four sources range from 0.1 $M_{\odot}$ to 0.39 $M_{\odot}$, assuming a dust temperature of 25 K for protostellar condensations (E2_A and E2_B) and 10 K for starless condensations (E2_C and E2_D). The gas masses of E2_C (∼0.39 $M_{\odot}$) and E2_D (∼0.19 $M_{\odot}$) are larger than their M_{vir}, indicating that the two condensations are likely gravitationally bound if they are as cold as 10 K (see Appendix A). Considering that no infrared or radio point sources have been detected toward E2_C and E2_D (Tobin et al. 2020), these two condensations are likely gas condensations in the prestellar phase Adopting a conservative star formation efficiency of 30% estimated on core scales (Motte et al. 1998; Offner & Chaban 2017), we predict that E2_C will have a final stellar mass slightly above the brown dwarf limit (80 Jupiter mass; ∼0.08 $M_{\odot}$) and that E2_D might form a brown dwarf. However, both E2_C and E2_D may experience a rapid collapse within such a small (∼200 au) region, resulting in a much higher in situ star formation efficiency. In addition, considering that E2_C and E2_D are embedded in continuum streamer-like structures (see Section 3.2), they might continue to accumulate gas from their surroundings. Therefore, both E2_C and E2_D may have potential to form a low-mass star.

As discussed in Appendix B, $C^{18}O$ $J = 2-1$ line emission is detected toward both E2_C and E2_D, but N_2D^+ $J = 3-2$ line emission, as well as other lines targeted by the ALMASOP project (e.g., DCN, DCO^+), are not detected. This may indicate that the two starless gas condensations are warmer than 10 K. If we assume a higher temperature of 25 K for E2_C and E2_D, their gas masses decrease by a factor of ∼4 and virial masses increase by a factor of ∼1.5 (see Appendix A). In this case, the two gas condensations will not be gravitationally bound and may disperse in future. However, the observed $C^{18}O$ $J = 2-1$ line emission does not resemble the continuum emission with compact structures, and is more likely related to the extended emission from the natal gas core at large scale. The nondetection of other lines is potentially due to the poor sensitivity and spectral resolution. Therefore, the two starless

[31] https://dendrograms.readthedocs.io/en/stable/

objects E2_C and E2_D may not be as warm as their protostellar counterparts in the system. Future enhanced-sensitivity line observations from multiple transitions of known temperature probes (such as NH_3, HC_3N, and CCS) are needed to better constrain the gas temperature of these objects.

To summarize, G206.93-16.61E2 thus forms a quadruple stellar system consisting of two protostars and two candidate gravitationally bound gas condensations. This system is more compact, having much smaller separations between components, than the quadruple system in the Barnard 5 dense core (Pineda et al. 2015).

3.2. Continuum "Ribbons" around Young Stellar Objects and Condensations

Figure 1(b) clearly shows the presence of continuum streamer-like structures connecting the four compact objects, and two of the sources (E2_A and E2_D) are associated with very elongated features within the core. We used the FilFinder Python package[32] to extract these elongated features from the mask created over $5\sigma_{1.3\,\mathrm{mm}}$ in the 1.3 mm dust continuum image. We adopt branch_thresh = 450 au, prune_criteria = "length." Three main continuum elongated structures (hereafter, "ribbons")[33]—S1, S2, and S3—are identified, which are marked as purple lines in Figure 1(b). The three branches of S1 are considered to be substructures by Filfinder. The projected lengths of these continuum ribbons are 700 au, 600 au, and 2200 au for S1, 500 au for S2, and 1500 au for S3.

The continuum ribbon S1 traverses both E2_A and E2_C, and bifurcates in the northern part of E2_C. The continuum ribbon S2 crosses through E2_B and may extend outward toward the western end of the continuum ribbon S3, while S3 connects E2_D with the tail of its envelope. Since the length of the continuum ribbon S2 is comparable with the size of E2_B and almost connects to S3, it may be a branch of S3 instead of a separate continuum ribbon. The continuum ribbons S1 and S3 converge into a hub region that forms E2_A, E2_C, and E2_D, suggesting that these compact objects could continuously accumulate gas along these features.

In previous studies, streamers have often been revealed by dense gas tracers, e.g., NH_3, HC_3N, and CCS (Alves et al. 2019; Yen et al. 2019; Pineda et al. 2020; Ren et al. 2020; Valdivia-Mena et al. 2022), while a few additional similar structures are traced by continuum emission (Pérez et al. 2016; Sanhueza et al. 2021). The three continuum ribbons in this system are clearly detected in the 1.3 mm dust emission. However, only a few molecular lines show weak emission at Band 6 in the ALMASOP observations (see Figure 5 in Appendix B), and none resemble the continuum emission. This may be due to both line excitation conditions and the sensitivity limit of the observations. Except for S2, the other two continuum ribbons, S1 and S3, extend to thousands of astronomical units in spatial scale and are likely formed by transporting material from the core to the protostars as funnels. These ribbons are likely only moderately heated by the embedded protostars, are expected to be cold, and may contain chemically fresh material (Pineda et al. 2020). Tatematsu et al. (2022) found that the HCO^+ spectra exhibited inverse P Cyg–like absorption profiles toward the G206.93-16.61E2 dense core, suggesting that the core itself is collapsing. This also indicates that these continuum ribbons likely trace gas accretion. Future observations of low-excitation lines, such as CCS and HC_3N, which trace chemically fresh material, may help to reveal the gas kinematics to see whether the ribbon structures are formed via large-scale accretion flows funneling material down to disk scales or not.

[32] https://github.com/e-koch/FilFinder

[33] We refer to the elongated structures seen in the dust continuum as "ribbons" rather than "streamers" in this work because we do not have complementary gas kinematic measurements associated with these structures.

3.3. Molecular Outflows

Recent studies have indicated that the outflows of multiple systems can have a great impact on the evolution of their member protostars (Jørgensen et al. 2022; Harada et al. 2023). In G206.93-16.61E2, the high-velocity ^{12}CO $J = 2-1$ line emission reveals an outflow structure spanning 24″ (∼9600 au) and consisting of two asymmetric, intricate, arc-like structures around the protostellar system, as shown in Figure 2. The systemic velocity of G206.93-16.61E2 is 9.8 km s^{-1} (Kim et al. 2020). To investigate the ^{12}CO $J = 2-1$ and C^{18}O $J = 2-1$ line emission, we define the velocity ranges of [−10, 2.6] km s^{-1} and [18, 29.2] km s^{-1} for the blue- and redshifted high-velocity components of the ^{12}CO $J = 2-1$ line wings (see Figure 2(b)). Figures 2(c) and (d) present the moment maps for the high-velocity emission of the ^{12}CO $J = 2-1$ line: integrated intensity (Moment 0) and intensity-weighted velocity (Moment 1).

We calculate outflow parameters such as mass ($M_{\rm out}$), momentum ($P_{\rm out}$), energy ($E_{\rm out}$), projected length ($\lambda_{\rm out}$), dynamic timescale ($t_{\rm dyn}$), and mass outflow rate ($\dot{M}_{\rm out}$) from the ^{12}CO $J = 2-1$ line wings. The resulting values are listed in Table 2. The formulae used and more details for these calculations are described in Appendix C. The total outflow mass and mass-loss rate are $3.1 \times 10^{-3}\,M_\odot$ and $2.5 \times 10^{-6}\,M_\odot$ yr^{-1}, respectively. These results are similar to outflow parameters detected in the Orion A cloud (Harada et al. 2023). Note, however, that we adopt the maximum projected length of each lobe as the outflow length ($\lambda_{\rm out}$). The actual lengths are larger than the projected value, thus resulting in a mass-loss rate that is an upper limit.

As shown in Figure 2(c), the outflow lobes do not exhibit a collimated bipolar outflow pattern. Instead, they appear to have divergent trajectories and arc-like structures. The outflow lobes are highly fragmented with strip and knot-like substructures. The overall morphology in G206.93-16.61E2 is reminiscent of the crescent-shaped structure of the pole-on outflow surrounding the protostar DK Cha (Harada et al. 2023). Given this, the complicated arc-like outflow structures in G206.93-16.61E2 may also indicate a nearly pole-on outflow cavity. The pole-on direction of the outflow is also evidenced by the orientation of the disk. Both E2_A and E2_B show nearly circular symmetric shapes in higher-resolution (∼40 au) continuum observations at 870 μm (Tobin et al. 2020), indicating that their disks are likely viewed face-on.

Although this source (G26.93-16.61E2) is located at the edge of the reflection nebula NGC2023 (see Figure 2(a)), the red and blue lobes of the outflow do not appear to follow the shell of the nebula, indicating that the outflow is very unlikely induced by the expansion of the nebula. As shown in Figures 2(c) and (d), the two detected young stellar objects (YSOs; E2_A and E2_B) are located close to the centers of the outflow lobes, and are thus likely candidate sources for driving the outflow. In particular, the protostar E2_A is much closer to

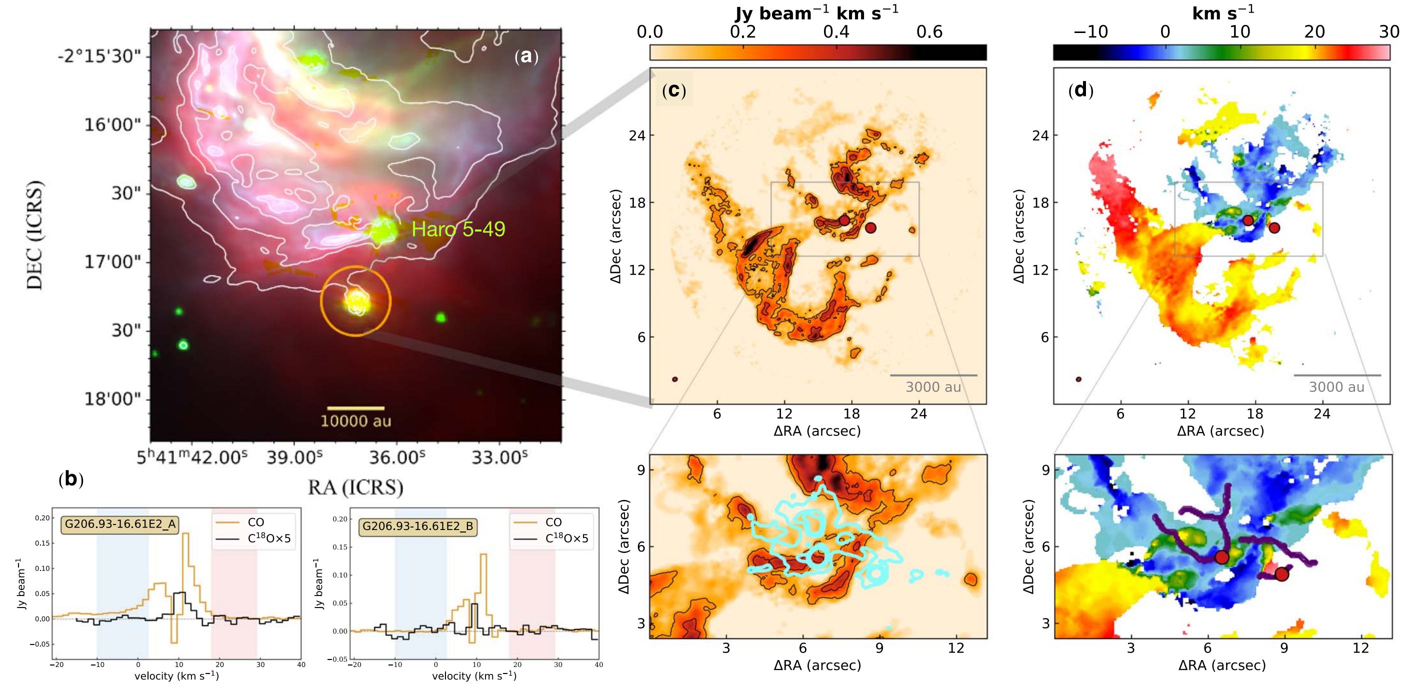

Figure 2. The CO outflow from G206.93-16.61E2. (a) The color image is the same as in Figure 1(a). The white contours show the Spitzer 8 μm emission. The orange circle shows the FOV of the ALMA image. (b) $C^{18}O$ and ^{12}CO $J = 2-1$ spectra at the positions of G206.93-16.61E2_A and G206.93-16.61E2_B. The blue and red shaded areas define the blue- and redshifted high-velocity emission of the ^{12}CO line emission. (c) Moment 0 map of all high-velocity emission combined ([−10 to 2.6] km s^{-1} for blue and [18 to 29.2] km s^{-1} for red), as defined in panel (b), with contours of $10\sigma_{\rm out}$ and $25\sigma_{\rm out}$ ($1\sigma_{\rm out} = 33$ mJy beam^{-1}). The zoom-in picture shows the same image, with dust continuum contours in cyan at $3\sigma_{1.3\ \rm mm}$, $10\sigma_{1.3\ \rm mm}$, and $20\sigma_{1.3\ \rm mm}$. (d) Moment 1 map of high-velocity emission. The red circles represent the protostars E2_A and E2_B. The structures of the continuum ribbons identified by Filfinder are shown with purple lines.

Table 2
Outflow Parameters of G206.93-16.61E2

Lobe (1)	$V_{\rm lsr}$ (km s^{-1}) (2)	Δv (km s^{-1}) (3)	$M_{\rm out}$ (10^{-2} $M_\odot$) (4)	$P_{\rm out}$ (10^{-2} $M_\odot$ km s^{-1}) (5)	$E_{\rm out}$ (10^{43} erg) (6)	$\lambda_{\rm out}$ (10^{-1} pc) (7)	$t_{\rm dyn}$ (10^4 yr) (8)	$\dot{M}_{\rm out}$ (10^{-5} $M_\odot$ yr^{-1}) (9)
Red	9.8	[18, 29.2]	0.18	2.16	0.14	0.36	1.37	0.13
Blue	9.8	[−10, 2.6]	0.13	1.56	0.10	0.32	1.07	0.12

the outflow origin and is likely the main driving source. The protostar E2_B may be associated with partial weak outflow emission, although it is hard to confirm, based on the current data. The complicated structure of the outflow may be produced by the dynamical evolution of the quadruple system or turbulent motions during its accretion phase (Offner et al. 2016), which could be tested in future state-of-the-art numerical simulations.

4. Discussion

Previous studies suggest that dynamical interactions among member stars can occur within star clusters/associations, potentially leading to the capture of members into bound systems (Howe & Clarke 2009). Such events are seen in recent numerical simulations, and these results widely show the presence of gas bridge streamers between protostars, which can be evidence for mutual interacting processes between the stellar systems (Kuffmeier et al. 2019; Lee et al. 2019).

Lee et al. (2019) simulated several turbulent star-forming clouds with different magnetic field strengths to study how multiple systems form and evolve. Their simulations form a number of higher-order multiple systems, including a gravitationally bound quadruple that appears to be a good analog to G206.93-16.61E2. This system forms in the strong magnetic field cloud ($B_{\rm rms} \sim 32$ μG). It has gas streamers and a hub–filament morphology, as shown in Figures 3(a) and (b). The lengths of the simulated gas streamer structures, 400–2500 au, are comparable to those in G206.93-16.61E2. In their simulation, two protobinary systems form via turbulent fragmentation and then merge to create a quadruple system, with the resulting streamers being a product of the interaction. Figure 3(a) shows that gas material is mainly flowing along the upper left streamers toward the protostars. The lower right streamers are likely to be sheared, with the close-in parts going inward and the rest moving outward. The gas flows along the major streamers are further illustrated with arrows in Figure 3(b).

Figures 3(c) and (d) display the synthetic 1.3 mm continuum observation of the quadruple system in the simulation (Lee et al. 2019). To compare with our observations, we simulated the 1.3 mm continuum emission assuming a dust temperature of 10 K and the optically thin continuum emission (more details are in Appendix D), using the CASA *simalma* task. We adopted the same antenna configurations (C43-2, C43-5, and ACA) and added thermal noise, as used for the actual observations. Additionally,

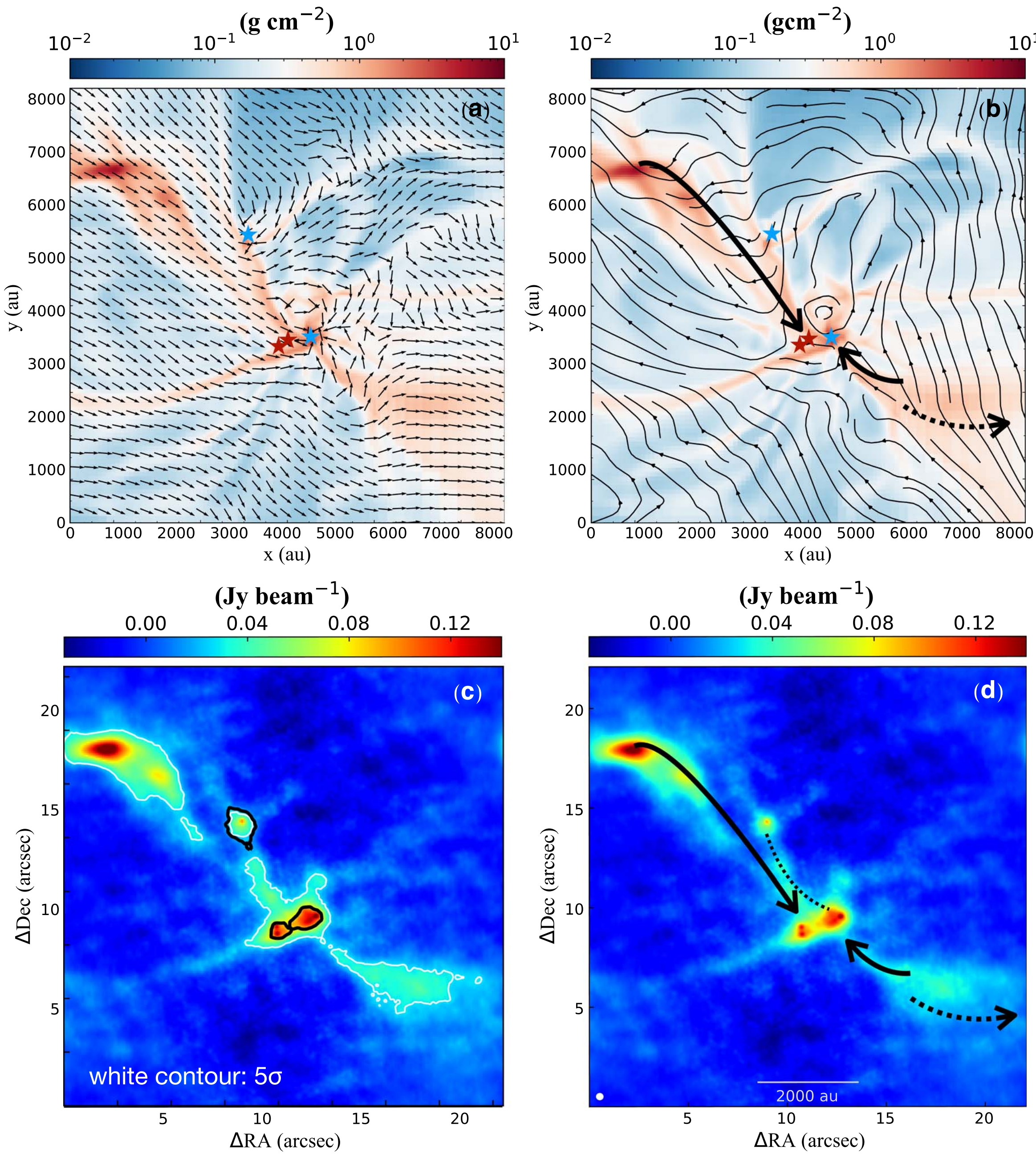

Figure 3. Image of a quadruple star system simulated in three dimensions and gravo-MHDs (Lee et al. 2019). (a) H_2 column density map with the density-weighted projected velocity vectors (black arrows). The star symbols represent the locations of the sink particles. Stars with the same colors were previously in a binary system. (b) The color image is the same as in panel (a). The black streamlines represent the density-weighted projected magnetic field. The black arrows indicate the direction of gas motion along the two major gas streamers. (c) Synthetic observation of the 1.3 mm dust continuum emission. The contour at 5σ is in white and the black contour represents the "leaf" structure identified by Astrodendro ($1\sigma = 5$ mJy beam^{-1}). (d) The color image is the same as in panel (c). The black solid lines with arrows represent the gas accretion flows along the streamers. The black dashed line marks a gas bridge connecting two protostars.

we added four point sources (0.1 Jy) representing protostars at the locations of the sink particles in Lee et al. (2019). Two of the point sources are unresolved in the synthetic observation. The masses of the point sources identified in the synthetic observations are 3.16, 1.37, and 1.47 $M_\odot$, respectively, which we note are more massive than those in G206.93-16.61E2. The "leaf" structures identified by Astrodendro in the synthetic observations are shown in black contours in Figure 3(c). These elongated structures surrounding point sources, as also seen in G206.93-16.61E2 (see Figure 1(b)), are likely shaped by the streamers around them. As seen in Figures 3(c) and (d), the synthetic observation of the 1.3 mm continuum clearly shows synthetic continuum-observed streamers of over the 5σ level around the protostars in the dust emission. The continuum streamer marked by the black dashed line in Figure 3(d) is a gas bridge connecting two protostars. The other continuum streamers marked by the black solid arrows extend over thousands of astronomical units, tracing gas accretion flows that in some cases are transporting material from the surroundings to the protostars.

Gas accretion along the upper left streamer is also evidenced by the pinched magnetic field, as shown in Figure 3(b). The magnetic field has been twisted along the accretion direction, as marked by the black arrow. Close to the densest part of the streamer, the magnetic field is compressed and is roughly perpendicular to its spine. The accretion significantly increases the perpendicular component of the magnetic field at the streamer, forming a U-shaped field geometry. Such a pinched magnetic field caused by gas accretion has been witnessed in both observations (Liu et al. 2018; Pillai et al. 2020) and other simulation works (Gómez et al. 2018). On the other hand, the magnetic field in the very central region is greatly distorted by gas accretion as well as interaction among member protostars. The magnetic field of the continuum ribbons in G206.93-16.61E2 could be investigated by high-sensitivity linear dust polarization observations with ALMA. With a continuum rms level of $\sim$10 μJy beam^{-1}, we expect to have a good detection of the linear polarization (signal-to-noise ratio > 3), even in its outer envelopes (>0.75 mJy beam^{-1} within the outer contours in the right panel of Figure 1), which would have high fractional polarization (5%–11%, such as in Cox et al. 2018 and Maury et al. 2018).

While this simulated system is not intended to replicate G206.93-16.61E2, their gas structures are remarkably similar. This supports the scenario that the continuum ribbons in G206.93-16.61E2 may act as accretion flows, and the continuum ribbon S2 and S3 may also function as a bridge connecting member protostars, resulting from gravitational drag as the members migrate toward each other. This scenario can be further tested by future high-sensitivity and high–spectral resolution molecular line and dust polarization observations, which can reveal the details of the gas motions and pinched magnetic field of these continuum-observed ribbons.

5. Conclusions

We have studied the young multiple stellar system G206.93-16.61E2, aiming to explore the formation mechanism of higher-order systems, using the ALMA 1.3 mm dust continuum and line emission data. The main results are summarized as follows:

1. G206.93-16.61E2 is forming a low-mass quadruple system. It contains two Class I protostellar sources and two candidate prestellar condensations. The four sources have separations smaller than 1000 au.
2. The 1.3 mm dust continuum emission reveals three distinct, asymmetric continuum ribbons with lengths ranging from 500 to 2200 au in G206.93-16.61E2. By comparing with MHD simulations, we suggest that these ribbons may trace gas accretion flows and also function as bridges connecting the members in this quadruple system. Future high-sensitivity and high–spectral resolution molecular line and dust polarization observations are needed to reveal the details of the gas motions and pinched magnetic field of these continuum-observed ribbons.
3. High-velocity ^{12}CO line emission reveals an asymmetric, complicated outflow containing substructures such as strips and knots. Its arc-like structures likely indicate a pole-on outflow cavity.

Acknowledgments

This paper makes use of the following ALMA data: ADS/JAO.ALMA#2018.1.00302.S. ALMA is a partnership of ESO (representing its member states), NSF (USA), and NINS (Japan), together with NRC (Canada), MOST and ASIAA (Taiwan), and KASI (Republic of Korea), in cooperation with the Republic of Chile. The Joint ALMA Observatory is operated by ESO, AUI/NRAO, and NAOJ. This work has been supported by the National Key R&D Program of China (No. 2022YFA1603101). T.L. acknowledges support from the National Natural Science Foundation of China (NSFC), through grants No. 12073061 and No. 12122307, the international partnership program of the Chinese Academy of Sciences, through grant No. 114231KYSB20200009, and the Shanghai Pujiang Program 20PJ1415500. S.S.R.O. and A.T.L. are supported in part by NSF 1748571. The simulations of Lee et al. (2019) were done at the Massachusetts Green High Performance Computing Center (GHPCC LoneStar5) and the Texas Advanced Computing Center (TACC Stampede2). D.J. is supported by NRC Canada and by an NSERC Discovery Grant. This research was carried out in part at the Jet Propulsion Laboratory, which is operated by the California Institute of Technology under a contract with the National Aeronautics and Space Administration (80NM0018D0004). X. L. acknowledges support from NSFC, No. 12203086, and CPSF, No. 2022M723278. P.S. was partially supported by a Grant-in-Aid for Scientific Research (KAKENHI Numbers JP22H01271 and JP23H01221) of the Japan Society for the Promotion of Science (JSPS). M.J. acknowledges support from the Academy of Finland, grant No. 348342. L.B. gratefully acknowledges support from the ANID BASAL project FB210003. D.S. acknowledges support from the Ramanujan Fellowship (SERB, Govt. of India) and PRL. D.W.T. wishes to thank the UK Science and Technology Facilities Council (STFC) for support under grant No. ST/R000786/1. K.T. was supported by JSPS KAKENHI (grant No. JP20H05645). N.H. acknowledges NSTC 110- 2112-M-001-048 and NSTC 111-2112-M-001-060 grants.W.K. was supported by the National Research Foundation of Korea (NRF) grant funded by the Korea government (MSIT) (NRF-2021R1F1A1061794). S.S. R.O. acknowledges support from NSF grants 1748571, 2107942, and 2107340.

Appendix A
Masses and Stability Analysis

We derive the masses of the four G206.93-16.61E2 members assuming that the 1.3 mm dust emission is optically thin, using the following formula:

$$M_{\rm gas} = \frac{S_\nu D^2}{\kappa_\nu B_\nu(T_{\rm dust})}, \quad \text{(A1)}$$

where S_ν is the flux density from the 1.3 mm continuum emission from the ALMASOP observation and D is the distance of 400 pc. κ_ν is the dust opacity per unit mass column density at 1.3 mm, and the parameters are adopted from Dutta et al. (2020). We assume that the dust temperature of the protostellar condensations E2_A and E2_B is $T_{\rm dust} = 25$ K. For the condensations E2_C and E2_D, based on their unknown evolutionary status, we derived the gas mass with $T_{\rm dust}$ ranging from 10 to 25 K.

To determine the virial mass, we adopt the N_2H^+ line width of the core obtained from Nobeyama 45 m observations to derive the total velocity dispersion of N_2H^+, $\sigma_{v_{\rm N_2H^+}} = \frac{\Delta V_{\rm N_2H^+}}{\sqrt{8\ln 2}} \sim 0.24$ km s^{-1}, where $\Delta V_{\rm N_2H^+}$ is the FWHM

Table 3
Physical Parameters of the Two Starless Gas Condensations

Source ID	T_{dust} = 10 K						T_{dust} = 25 K					
	σ_{TH}	σ_{NT} (km s^{-1})	σ_{3D}	M_{vir}	M_{gas} ($M_\odot$)	α	σ_{TH}	σ_{NT} (km s^{-1})	σ_{3D}	M_{vir}	M_{gas} ($M_\odot$)	α
G206.93-16.61E2_C	0.20	0.24	0.54	0.18	0.39	0.46	0.32	0.23	0.68	0.29	0.11	2.63
G206.93-16.61E2_D	0.20	0.24	0.54	0.19	0.19	1.00	0.32	0.23	0.68	0.30	0.05	6.00

from Kim et al. (2020). Given that the N_2H^+ data have a much larger beam size, of ∼19″, than those of ALMA, which cover a large portion of the dense core, the derived three-dimensional gas line width should be treated as an upper limit in the following virial analysis for the gas condensations detected by ALMA. Assuming a density profile $\rho \propto r^{-1.5}$, we calculate the virial masses of the gas condensations following Williams et al. (1994):

$$M_{vir} = \frac{5R\sigma_{v_{3D}}^2}{3\gamma G}, \quad (A2)$$

where G is the gravitational constant, $\gamma = \frac{4}{5}$ when $\rho \propto r^{-1.5}$, and R is the deconvolved radius of each member provided by Astrodendro, following the procedure of Xu et al. (2023). $\sigma_{v_{3D}}$ is the three-dimensional velocity dispersion for the H_2 gas, $\sigma_{v_{3D}} = \sqrt{3(\sigma_{TH}^2 + \sigma_{NT}^2)}$. The thermal velocity dispersion of the H_2 gas is $\sigma_{TH} = \sqrt{\left(\frac{k_b T_k}{m_H \mu}\right)}$, where k_b is the Boltzmann constant, T_k is the kinetic temperature, m_H is the hydrogen mass, and μ is the molecular weight of the H_2. The nonthermal velocity dispersion, σ_{NT}, is derived from the FWHM of the N_2H^+ line width, given by $\sigma_{NT} = \sqrt{\sigma_{v_{N_2H^+}}^2 - \sigma_{TH,N_2H^+}^2}$. The thermal velocity dispersion of N_2H^+ (σ_{TH,N_2H^+}) is derived by assuming a gas temperature ∼10–25 K. The velocity dispersion, gas masses, and virial masses for the two starless gas condensations E2_C and E2_D are summarized in Table 3.

The virial parameter α of each member is derived using the equation

$$\alpha = M_{vir}/M_{gas}. \quad (A3)$$

A source is gravitationally bound if $\alpha < 2$ (Kauffmann et al. 2013). For the condensations E2_C and E2_D, the gas mass M_{gas} and the virial parameter α are calculated for two different dust temperature conditions. We list the derived values for M_{gas} and α at 10 and 25 K in Table 3.

Figure 4 shows the virial parameters as a function of dust temperature for the four gas condensations. E_A and E2_B have been classified as Class I protostars. The virial parameter of E2_A is below 2, while E2_B is above 2. Since we do not take into account their stellar masses, the virial parameters of E2_A and E2_B should be overestimated. For the two starless condensations E2_C and E2_D, their virial parameters increase as the dust temperature increases. Their virial parameters exceed the boundary of $\alpha = 2$ at ∼14 K and ∼22 K, respectively. The accurate temperatures and corresponding virial parameters of E2_C and E2_D should be further constrained in future observations.

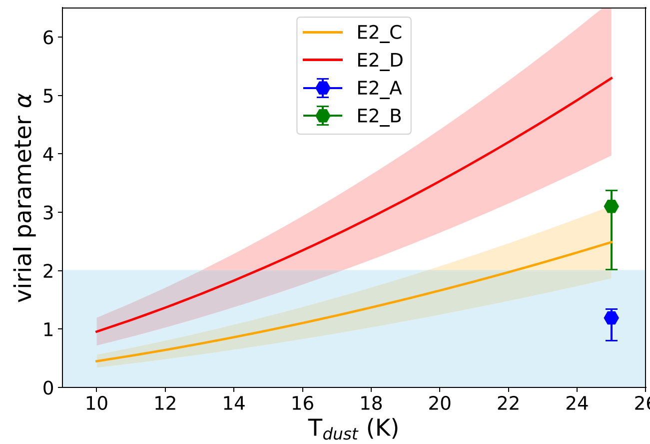

Figure 4. The dust temperature vs. virial parameter for the four gas condensations in G206.93-16.61E2. The blue and green polygons with error bars denote the virial parameters of E2_A and E2_B at 25 K, respectively. The orange and red lines with hatched regions show the corresponding virial parameters and dust temperature T_{dust} values ranging from 10 to 25 K. The lines correspond to the good model for describing infalling envelopes $\rho \propto \gamma^{1.5}$. The hatched regions and error bars correspond to the the density profile models from $\rho \propto \gamma^0 - \gamma^2$. The blue regions highlight the virial parameters $\alpha \leqslant 2$ that indicate a gravitationally bound status.

Appendix B
Molecular Line Emission

Figure 5 presents the integrated intensity maps for $C^{18}O$ $J = 2-1$, SiO $J = 5-4$, and H_2CO $J = 3-2$. These emission maps do not have a direct correspondence to the continuum "ribbons." The $C^{18}O$ emission exhibits an extended feature and does not show any compact emission that is associated with the four gas condensations, indicating that its emission may originate from the large-scale natal gas core. The emission from both SiO and H_2CO is concentrated to the north of the continuum emission, potentially denoting a shell-like structure that may be induced by outflow shocks.

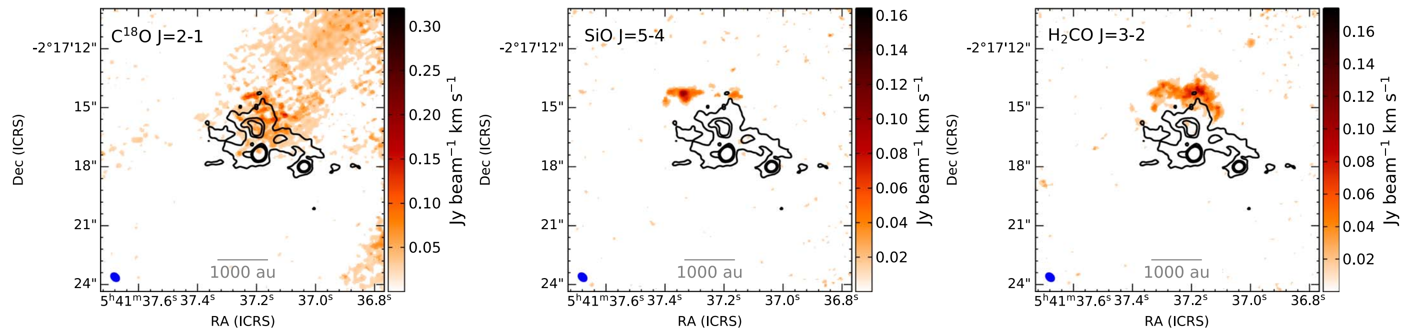

Figure 5. Integrated intensity maps of C^{18}O, SiO, and H_2CO emission, with the dust continuum in black contours at $3\sigma_{1.3\text{ mm}}$, $10\sigma_{1.3\text{ mm}}$, and $20\sigma_{1.3\text{ mm}}$.

Appendix C
Physical Properties of the Outflow

To estimate the physical properties of the outflow, we assume that high-velocity CO emission is optically thin and use the following equations to calculate the outflow parameters: outflow mass ($M_{\rm out}$), momentum ($P_{\rm out}$), energy ($E_{\rm out}$), dynamic timescale ($t_{\rm dyn}$), projected length ($\lambda_{\rm out}$), and mass outflow rate ($\dot{M}_{\rm out}$; Qiu et al. 2009; Li et al. 2020):

$$M_{\rm out} = 1.36 \times 10^{-6} \exp\left(\frac{16.59}{T_{\rm ex}}\right) \times (T_{\rm ex} + 0.92) D^2 \int \frac{\tau_{12}(1 - e^{-\tau_{12}})}{S_\nu} d\nu;$$

$$P_{\rm out} = \sum M_{\rm out}(v) v;$$

$$E_{\rm out} = \frac{1}{2} \sum M_{\rm out}(v) v^2;$$

$$t_{\rm dyn} = \frac{\lambda}{(v_{\max(b)} + v_{\max(r)})/2};$$

$$\dot{M}_{\rm out} = \frac{M_{\rm out}}{t_{\rm dyn}}.$$

Here, we assume the excitation temperature $T_{\rm ex} = 30$ K, D represents the distance in kpc ~ 0.40 pc, $M_{\rm out}$ has a unit of $M_\odot$, S_ν is the flux density from the ^{12}CO emission, and $v_{\max}$ is the maximum velocity of each lobe.

Appendix D
Flux Density of the Simulated Data

The 1.3 mm flux density is determined using the H_2 column density (Kauffmann 2007), N_{H_2}, assuming the dust to be optically thin, i.e.,

$$F_\nu = 2.02 \times 10^{-20} \text{ cm}^{-2} (e^{1.439(\lambda/\text{mm})^{-1}(T/10\text{ K})^{-1}} - 1)^{-1} \times \left(\frac{\lambda}{\text{mm}}\right)^{-3} \left(\frac{\kappa_\nu}{0.01 \text{ cm}^2 \text{ g}^{-1}}\right) \left(\frac{\theta_{\rm pixel}}{10''}\right)^2 \times N_{H_2}.$$

Here, F_ν has a unit of Jy pixel^{-1}, λ is the wavelength of the continuum in mm, $T_{\rm dust}$ is the dust temperature, which we assume is 10 K, κ_ν is the dust opacity from Equation (A1), and $\theta_{\rm pixel}$ is the angular pixel size.

ORCID iDs

Qiu-yi Luo https://orcid.org/0000-0003-4506-3171
Tie Liu https://orcid.org/0000-0002-5286-2564
Aaron T. Lee https://orcid.org/0000-0002-8428-8050
Stella S. R. Offner https://orcid.org/0000-0003-1252-9916
James di Francesco https://orcid.org/0000-0002-9289-2450
Doug Johnstone https://orcid.org/0000-0002-6773-459X
Mika Juvela https://orcid.org/0000-0002-5809-4834
Paul F. Goldsmith https://orcid.org/0000-0002-6622-8396
Sheng-Li Qin https://orcid.org/0000-0003-2302-0613
Xiaofeng Mai https://orcid.org/0000-0001-7573-0145
Xun-chuan Liu https://orcid.org/0000-0001-8315-4248
Patricio Sanhueza https://orcid.org/0000-0002-7125-7685
Feng-Wei Xu https://orcid.org/0000-0001-5950-1932
Ken'ichi Tatematsu https://orcid.org/0000-0002-8149-8546
Somnath Dutta https://orcid.org/0000-0002-2338-4583
Huei-Ru Vivien Chen https://orcid.org/0000-0002-9774-1846
Shanghuo Li https://orcid.org/0000-0003-1275-5251
Aiyuan Yang https://orcid.org/0000-0003-4546-2623
Sheng-Yuan Liu https://orcid.org/0000-0003-4603-7119
Chin-Fei Lee https://orcid.org/0000-0002-3024-5864
Naomi Hirano https://orcid.org/0000-0001-9304-7884
Chang Won Lee https://orcid.org/0000-0002-3179-6334
Dipen Sahu https://orcid.org/0000-0002-4393-3463
Hsien Shang https://orcid.org/0000-0001-8385-9838
Shih-Ying Hsu https://orcid.org/0000-0002-1369-1563
Leonardo Bronfman https://orcid.org/0000-0002-9574-8454
Woojin Kwon https://orcid.org/0000-0003-4022-4132
M. G. Rawlings https://orcid.org/0000-0002-6529-202X
David Eden https://orcid.org/0000-0002-5881-3229
Xing Lu https://orcid.org/0000-0003-2619-9305
Zhiyuan Ren https://orcid.org/0000-0003-4659-1742
D. Ward-Thompson https://orcid.org/0000-0003-1140-2761
Zhi-Qiang Shen https://orcid.org/0000-0003-3540-8746

References

Alves, F. O., Caselli, P., Girart, J. M., et al. 2019, Sci, 366, 90
Chen, X., Arce, H. G., Zhang, Q., et al. 2013, ApJ, 768, 110
Clark, P. C., Glover, S. C. O., Smith, R. J., et al. 2011, Sci, 331, 1040
Cox, E. G., Harris, R. J., Looney, L. W., et al. 2018, ApJ, 855, 92
Dong, R., Liu, H. B., Cuello, N., et al. 2022, NatAs, 6, 331
Duchêne, G., & Kraus, A. 2013, ARA&A, 51, 269
Dutta, S., Lee, C.-F., Liu, T., et al. 2020, ApJS, 251, 20
Furlan, E., Fischer, W. J., Ali, B., et al. 2016, ApJS, 224, 5
Gómez, G. C., Vázquez-Semadeni, E., & Zamora-Avilés, M. 2018, MNRAS, 480, 2939
Harada, N., Tokuda, K., Yamasaki, H., et al. 2023, ApJ, 945, 63
Howe, K. S., & Clarke, C. J. 2009, MNRAS, 392, 448
Jørgensen, J. K., Kuruwita, R. L., Harsono, D., et al. 2022, Natur, 606, 272

Kauffmann, J. 2007, PhD thesis, Max-Planck-Institute for Radioastronomy, Bonn
Kauffmann, J., Pillai, T., & Goldsmith, P. F. 2013, ApJ, 779, 185
Keppler, M., Penzlin, A., Benisty, M., et al. 2020, A&A, 639, A62
Kim, G., Tatematsu, K., Liu, T., et al. 2020, ApJS, 249, 33
Kounkel, M., Covey, K., Suárez, G., et al. 2018, AJ, 156, 84
Kounkel, M., Megeath, S. T., Poteet, C. A., Fischer, W. J., & Hartmann, L. 2016, ApJ, 821, 52
Kratter, K. M., Matzner, C. D., Krumholz, M. R., & Klein, R. I. 2010, ApJ, 708, 1585
Kuffmeier, M., Calcutt, H., & Kristensen, L. E. 2019, A&A, 628, A112
Kwon, W., Fernández-López, M., Stephens, I. W., & Looney, L. W. 2015, ApJ, 814, 43
Lee, A. T., Offner, S. S. R., Kratter, K. M., Smullen, R. A., & Li, P. S. 2019, ApJ, 887, 232
Li, S., Sanhueza, P., Zhang, Q., et al. 2020, ApJ, 903, 119
Liu, T., Li, P. S., Juvela, M., et al. 2018, ApJ, 859, 151
Luo, Q.-y., Liu, T., Tatematsu, K., et al. 2022, ApJ, 931, 158
Maury, A. J., Girart, J. M., Zhang, Q., et al. 2018, MNRAS, 477, 2760
McMullin, J. P., Waters, B., Schiebel, D., Young, W., & Golap, K. 2007, in ASP Conf. Ser. 376, Astronomical Data Analysis Software and Systems XVI, ed. R. A. Shaw, F. Hill, & D. J. Bell (San Francisco, CA: ASP), 127
Megeath, S. T., Gutermuth, R., Muzerolle, J., et al. 2012, AJ, 144, 192
Motte, F., Andre, P., & Neri, R. 1998, A&A, 336, 150
Offner, S. S. R., & Chaban, J. 2017, ApJ, 847, 104
Offner, S. S. R., Dunham, M. M., Lee, K. I., Arce, H. G., & Fielding, D. B. 2016, ApJL, 827, L11
Offner, S. S. R., Moe, M., Kratter, K. M., et al. 2022, arXiv:2203.10066
Oya, Y., Watanabe, Y., López-Sepulcre, A., et al. 2021, ApJ, 921, 12
Pérez, L. M., Carpenter, J. M., Andrews, S. M., et al. 2016, Sci, 353, 1519
Pillai, T. G. S., Clemens, D. P., Reissl, S., et al. 2020, NatAs, 4, 1195
Pineda, J. E., Offner, S. S. R., Parker, R. J., et al. 2015, Natur, 518, 213
Pineda, J. E., Segura-Cox, D., Caselli, P., et al. 2020, NatAs, 4, 1158
Qiu, K., Zhang, Q., Wu, J., & Chen, H.-R. 2009, ApJ, 696, 66
Ren, B., Dong, R., van Holstein, R. G., et al. 2020, ApJL, 898, L38
Rosotti, G. P., Benisty, M., Juhász, A., et al. 2020, MNRAS, 491, 1335
Sahu, D., Liu, S.-Y., Johnstone, D., et al. 2023, ApJ, 945, 156
Sahu, D., Liu, S. Y., Liu, T., et al. 2021, ApJ, 907, L15
Sanhueza, P., Girart, J. M., Padovani, M., et al. 2021, ApJL, 915, L10
Takakuwa, S., Saigo, K., Matsumoto, T., et al. 2017, ApJ, 837, 86
Tatematsu, K., Yeh, Y.-T., Hirano, N., et al. 2022, ApJ, 931, 33
Tobin, J. J., Looney, L. W., Li, Z.-Y., et al. 2016, ApJ, 818, 73
Tobin, J. J., Offner, S. S. R., Kratter, K. M., et al. 2022, ApJ, 925, 39
Tobin, J. J., Sheehan, P. D., Megeath, S. T., et al. 2020, ApJ, 890, 130
Valdivia-Mena, M. T., Pineda, J. E., Segura-Cox, D. M., et al. 2022, A&A, 667, A12
Williams, J. P., de Geus, E. J., & Blitz, L. 1994, ApJ, 428, 693
Xu, F.-W., Wang, K., Liu, T., et al. 2023, MNRAS, 520, 3259
Yen, H.-W., Gu, P.-G., Hirano, N., et al. 2019, ApJ, 880, 69
Yi, H.-W., Lee, J.-E., Liu, T., et al. 2018, ApJS, 236, 51